International Journal of Heat and Mass Transfer 91 (2015) 848–860

Contents lists available at ScienceDirect

International Journal of Heat and Mass Transfer

journal homepage: www.elsevier.com/locate/ijhmt

Convective heat transfer investigation of acoustically excited flow over an isolated rib obstacle

Beni Cukurel *, Claudio Selcan, Maximilian Stratmann

Turbomachinery and Heat Transfer Laboratory, Technion-Israel Institute of Technology, Technion City, Haifa 32000, Israel

ARTICLE INFO

Article history:
Received 17 February 2015
Received in revised form 7 July 2015
Accepted 8 July 2015

Keywords:
Convective heat transfer
Standing sound wave
Traveling sound wave
Acoustic resonance
Shear layer modification
Flow reattachment
Fence flow
Rib roughened internal cooling

ABSTRACT

The research effort investigates the aero-thermal ramifications of acoustically excited turbulent reattaching shear flow in the wake of an isolated fence obstacle. In order to contrast the effectiveness of traveling and standing sound wave excitations towards surface heat transfer modulation, the flow is stimulated with forcing frequencies and amplitudes, in the ranges of 70–270 Hz (St = 0.1–0.38) and 103–131 dB respectively. Along with local static pressure measurements, the consequent convective heat transfer distributions are quantified by liquid crystal thermometry. Subjected to a standing wave (resonance conditions) within a conductive Strouhal regime in the St = 0.17–0.22 range, the separated flow behind the rib is observed to be significantly affected. This is evidenced by size reduction in the time averaged reattachment length of up to 37%. The ensuing local heat transfer enhancement is ~25%. Conversely, when the flow is excited with acoustic frequencies which do not correspond to resonances (traveling wave forcing), the local heat transfer distributions remained unchanged; however, limited variations in local static pressure are observed. For conditions that yield improved thermal performance, a minimum source amplitude threshold (~121 dB) is found; above this level, the aero-thermal effectiveness of the forcing rises monotonously with increased sound pressure. Even under thermally favorable excitation conditions, the integral pressure drop penalty (total net loss) remains invariant.

1. Introduction

Active and passive means of flow control are commonly employed in a broad range of applications towards deliberate modification of laminar and turbulent aerodynamic phenomena, including control of transition, boundary layer separation, shear-layer instability and flow reattachment [1,2]. A well-established approach is the introduction of small amplitude periodic disturbances to the flow. Perturbations are induced either globally (e.g. acoustic) or locally (synthetic jets, mechanical flaps, plasma actuators) [1]. The common concept underlying these flow control strategies is the deliberate manipulation of downstream shear flow evolution. Owing to its fundamental nature, flow control over a backward-facing step has received significant attention in the research community [3,4].

1.1. Rib roughened flow field

The isolated rib obstacle, comprising of a forward and rearward step, represents a generic/simple geometry incorporating various structures present in complex separating and reattaching flows. Internal passage flow over a fence is driven by the characteristic sequence of an abrupt contraction, followed by a sudden expansion. The obstacle's potential effect on the upstream flow leads to an initial acceleration and deviation away from the near wall. Hence, the free shear layer formation is initiated upstream of the fence. A prominent flow separation region in the wake of the rib dominates the flow field. In Fig. 1, time-averaged PIV streamlines and streamwise velocity magnitudes at Re_H = 12.000 and BR = 30% show that the shear layer has the effect of bounding the low-momentum vortex cell atop the rib and confining the flow recirculation bubble in the wake of the fence. Shear layer impingement on the bottom wall marks the point of flow reattachment x_R, in the vicinity of which local maximum heat transfer x_{max} occurs [5]. Downstream, the flat plate boundary layer redevelopment is initiated.

1.2. Shear layer dynamics

The physical processes associated with the initial free shear region directly downstream of the step resembles a plane mixing layer - flow between two parallel streams at different velocities [2,7]. The mixing layer dynamics are governed by shear-induced vorticity and turbulence. As instability waves swirl into vortices, they give rise to spanwise-correlated coherent structures [8–11].

* Corresponding author.

http://dx.doi.org/10.1016/j.ijheatmasstransfer.2015.07.043
0017-9310/

Nomenclature

Symbol	Description
λ	[nm] sound wavelength
a	[m/s] air speed of sound
D_h	[m] channel hydraulic diameter
f	[Hz] sound frequency
h	[W/m^2 K] heat transfer coefficient
H	[m] fence height
k	[W/mK] air thermal conductivity
l	[m] characteristic length scale
M	[–] mach number
p	[Pa] pressure
Nu_D	[–] Nusselt number $[h(x,y) \cdot D_h/k]$
Re	[–] Reynolds number
St	[–] Strouhal number $[f \cdot H/U_\infty]$
SPL	[dB] sound pressure level
T	[K] temperature
x,y	[m] axial, lateral direction
u	[m/s] axial velocity

Abbreviation

BFS	backward-facing step
BR	channel blockage ratio
TLC	thermochromic liquid crystal

Subscript

0	acoustic source
∞	freestream conditions
D	hydraulic diameter based
H	step height based
max	maximum heat transfer
R	flow reattachment

Developing into sequential vortex pairing interactions, the growing scales asymptotically approach the local mixing layer thickness [11,12], and control the spreading rate as well as the entrainment of momentum.

These mechanisms also apply to the reattaching free shear layer, a consequence of flow separation over the fence [13]. Further downstream, the shear layer curves downward, followed by consequent impingement onto the wall. Beyond the flow reattachment region, vortex merging is inhibited due to the bounding surface [14–16]. However, due to persistence of large-scale coherent structures in the stream, the redevelopment of the conventional boundary layer is delayed [15,16].

1.3. Shear layer modulation

In literature, it has been observed that the shear layer dynamics can be strongly affected by periodic forcing via mechanical flaps, oscillating jets, acoustic excitation etc. In a broad range of conducive frequencies (typically reported in form of local Strouhal numbers), periodic forcing entails higher spreading rates with altered velocity profiles due to stimulation and organization of the vortex merging process. In the scope of reattaching free shear layers, this enhanced transverse momentum entrainment and mixing can result in an earlier reattachment and narrowed recirculation region [4,17,18].

In a detailed study of the forced plane mixing layer, Ho and Huang [9] ascertained frequency ranges conducive to higher spreading rates to be determined by the ratio of the shear layer natural instability frequency and the excitation frequency. Forcing at an integer subharmonic of the vortex passage frequency was found to be effective towards the vortex merging and mixing layer thickness control. The subsequently increased spreading rates were induced by a collective interaction that bypasses sequential pairing stages and merges multiple vortices simultaneously. In a

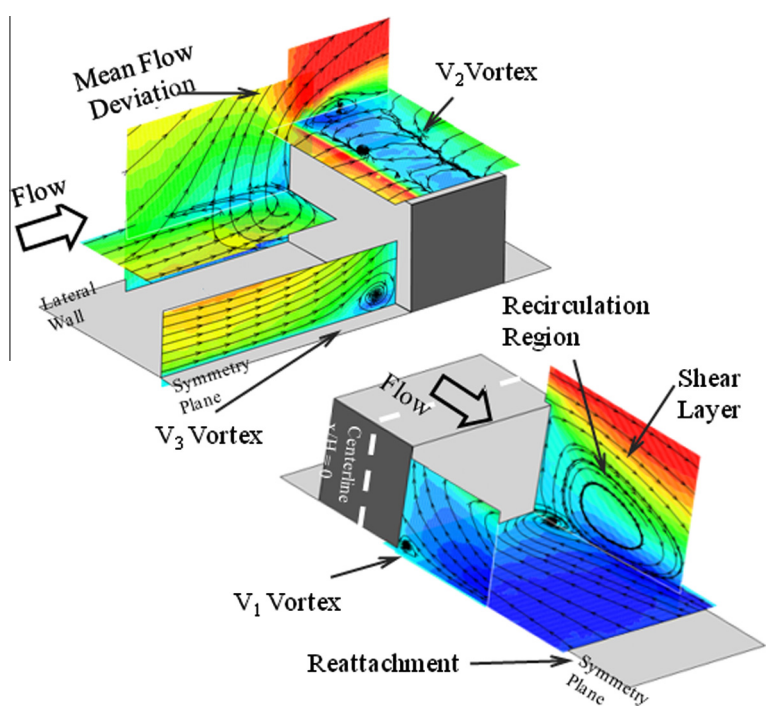

Fig. 1. Representative time-averaged fence-flow field at BR = 0.3, Re_H = 12,000; reproduced from [6].

similar study, using a local mechanical excitation upstream of the splitter plate edge, plane mixing layer's receptivity to subharmonic forcing below the natural shedding frequency was further corroborated by Oster and Wygnanski [17].

Building upon these fundamental physics, Bhattacharjee et al. [4] investigated the aerodynamic implications of forcing induced reattaching flow modulation in a turbulent backward facing step (BFS) geometry. A traveling sound wave excitation was employed from the opposite side of the expansion. In the Strouhal number range St = 0.1–0.4, the harmonic forcing below the natural vortex passage frequency was reported to accelerate vortex merging, which yielded higher transverse momentum entrainment and reduced the reattachment length by 10–15%. Moreover, turbulent fluctuations upstream of reattachment were observed to increase noticeably. In a similar BFS study, Roos and Kegelman [3] excited the flow at the dominant shedding frequency (St = 0.29) by a local flap located on the step edge. The regularization of spanwise-correlated structures was observed by the concentration of the formerly distributed velocity fluctuation energy into a sharp peak. The turbulent separation length was reduced up to 30%.

In a more complex fence flow environment, Siller and Fernholz [19] excited the flow upstream of the rib by a local flap and oscillating jet, which were situated on the same side wall as the obstacle. In the Strouhal range St = 0–0.25, both types of flow manipulation generated spanwise vortices at the fence that advected downstream and enhanced the shear layer mixing. Optimal Strouhal numbers around St = 0.05 and St = 0.15–0.25 were reported. Interestingly, while the time mean length of the reverse-flow region was reduced, the length of the region where instantaneous reverse-flow occurs remained unchanged.

Evidently, manipulating the vortex merging process and observing the phenomenological implications in a wide frequency band, the prior literature in the topic focused on exciting the reattaching flow by means of local sources and traveling sound waves.

1.4. Resonance effects in attached flows

Through reflection and constructive interference of traveling waves at the resonance condition, spatially-stationary and temporally-oscillating static pressure field of standing sound waves can be achieved. In attached flows, the effects of standing sound waves on the turbulent forced convection were demonstrated for longitudinal (streamwise oriented) acoustic resonance modes in straight duct and pipe geometries [20–24]. The flow field and heat transfer signatures reflect local imprints of resonance mode shape patterns, which were related to the flow Reynolds number. In the boundary layer, the streamwise formation of distinct vortex cells is reported. At low Reynolds numbers ($Re \leqslant 35{,}000$), regions of locally elevated and reduced heat transfer were reported to coincide with the pressure nodes and antinodes respectively. Conversely, at higher Reynolds numbers ($Re > 35{,}000$), locations of Nusselt number maxima and minima appear inversed, coinciding with the locations of velocity nodes and antinodes [24]. From a global perspective, the average convective heat transfer was found to be unaffected by standing sound waves at low Re, whereas a high Re lead to global heat transfer reduction [24]. However, other studies have indicated a rise in global heat transfer, inducing augmentations as large as 50% and 20% in laminar and turbulent attached flow respectively [25,26].

1.5. Resonance effects in separating flows

For the more complex case of separating flows subjected to acoustic resonances, only a limited number of studies exist and they analyze this problem in the scope of airfoil stall control [27–29]. Ahuja and Burrin [27,28] investigated turbulent separating boundary layer flow over an airfoil at high $Re \approx 700{,}000$ in a wide forcing range (70–165 dB – 0.4–5 kHz). At different angles of attack, notable excitation impact at distinct frequencies was found to delay and even suppress flow separation imposed by the adverse pressure gradient. The formation and alteration of large scale vortex structures in the separating shear layer was observed [27,28]. Deep stall severity was reported to be significantly mitigated at conducive forcing frequencies which were shown to coincide with acoustic resonance modes of the facility [29].

Zaman et al. [29] focused on laminar airfoil flow (Re = 40,000–150,000) at much lower SPL (104 dB). In contrast to traveling waves, more pronounced influence was observed with longitudinal and transverse resonance mode excitations. The impact of standing waves was demonstrated to be superior to off-resonance excitation with higher SPL [29]. The largest aerodynamic ramifications resulted from a transverse resonance, which induced a pressure node on the airfoil such that the greatest perturbation velocity was exerted normal to the model.

As indicated, the implications of standing sound waves on separating boundary layers were only analyzed in the scope of aerodynamic analysis over airfoils.

1.6. Motivation

On a fundamental level, prior investigations have demonstrated that periodic forcing of separated shear layers can be conducive towards alteration of the unsteady vortex dynamics. Although the underlying physical mechanisms are characterized from an aerodynamic perspective, only a small number of studies relate to the ensuing convective heat transfer ramifications. In the presence of highly unsteady instantaneous flow features, as the temporally averaged heat transfer does not necessarily directly correlate with time-mean aerodynamic fields, the subsequent impact on local surface heat exchange is not obvious.

Moreover, the literature on separated flow control mostly pertain to local excitations via mechanical devices, which deliver a large concentrated and localized energy input. However, this is impractical in closely confined heat exchange surfaces. Addressing this issue, there exists a modest amount of scientific effort addressing the subject of globally excited backward-facing step geometries, however the focus is predominantly on the purely aerodynamic perspective of traveling waves. Boundary layer control by acoustic resonance was only demonstrated in the scope of adverse pressure gradient airfoil flow separation so far.

Extending upon this knowledgebase, the current research investigates the convective heat transfer ramifications of sound excitation on a rib roughened flow topology. Through parametric frequency variations, the thermal effectiveness of standing (resonance) and traveling sound wave excitations are contrasted. Towards a generalized understanding, the study investigates whether forcing effectiveness is determined by the presence of a fixed acoustic eigenfrequency, or if it is the result of a traveling wave excitation in a favorable Strouhal regime. Furthermore, at conducive forcing conditions, the implications of excitation amplitude variation are examined.

2. Experimental methodology

2.1. Wind tunnel facility

The experimental wind tunnel facility employed is operated by a centrifugal blower running in aspiration mode; it is decoupled from the test section to damp out mechanical vibrations. Pressure fluctuation propagation from the driving unit is prevented by a settling chamber, equipped with two layers of fine mesh structures. The duct which forms the test and exhaust sections has a

20×20 cm cross section at a length of 4 m. Upstream, the air is sucked in through a bellmouth inlet of contraction area ratio 25:1, which was designed based on the guidelines proposed in Ref. [30]. The inlet is further equipped with a honeycomb and metal screen structure to attain minimum inflow swirl and to diminish spatial non-uniformities.

For setting the aerodynamic operating conditions along the channel, bulk velocity is measured via a Paragon duct mounted airflow measurement station, along with six T-type thermocouples exposed to freestream air at the test section inlet and outlet. The facility schematic can be found in Fig. 2.

The test section comprises of 1.5 m long Plexiglas walls which are supported by an aluminum frame. Optical access is enabled from two sides as one wall serves as the heat transfer investigation surface. Situated perpendicular to the mean flow, a single, squared wooden rib element with sharp edges is placed 57 cm downstream of the test section inlet, producing a channel blockage ratio of $H/D_h = 7.5\%$. The steady pressure distributions are acquired by pressure taps located along the channel wall centerline.

A Mackie DLM-8 loudspeaker (zero mass flow) is employed as the active audible frequency range excitation source (65 Hz–20 kHz), placed in a sealed casing on the observation side wall. A squared taut fine steel wire mesh (25 μm cell size), covering the entire 20 cm duct height, enables the acoustic excitations to permeate into the test section with minimal distortion of the channel flow, Fig. 4. Acoustic boundary conditions are acquired by a high-sensitivity wide frequency range (4 Hz–70 kHz) pressure field condenser microphone (type G.R.A.S. 46BD), flush mounted to the heat transfer surface side wall at the centerline. The signal is amplified with an Endevco Meggitt Model 133 conditioner, followed by acquisition via National Instruments NI 9205 module at 200 kS/s sampling rate and subsequent Fast Fourier Transform spectral analysis.

2.2. Identification of resonance frequencies

In order to identify relevant acoustic eigenfrequencies of the wind tunnel in the 100–200 Hz range, the facility's response to sound forcing is analyzed. Spanning a distance of 30–135 cm downstream of the inlet mesh, unsteady pressure measurements are conducted along the channel wall center-plane. Within the 70–270 Hz frequency range, the sound pressure level distributions at the only two resonant frequencies are charted in Fig. 3 (122 Hz and 167 Hz). The spatial variation and apparent node/antinode patterns is indicative of the characteristic longitudinal standing wave behavior. The sound pressure node of 122 Hz is seen to be induced at around 0.8 m, while corresponding antinodes are located further upstream and downstream by 0.5 m. In the case of 167 Hz excitation, the longitudinal mode shape pattern is shifted and the associated pressure node is situated 0.2 m ahead of the 122 Hz resonance node, thus moving closer to the rib obstacle located at 0.57 m.

Moreover, depending upon the location throughout the test section, the standing sound wave-induced SPL for 122 Hz and 167 Hz excitations are of similar magnitude. In both resonance excitation cases, the rib-roughened flow is subjected to the strong direct influence of acoustic pressure/velocity fluctuations.

2.3. Liquid crystal thermometry

Measurement of time-averaged convective heat transfer is conducted by means of wide-band liquid crystal thermometry at steady state. This allows optical acquisition of high-resolution spatial distributions of surface temperature and heat transfer coefficient. Cholesteric micro-encapsulated TLCs, type R35C20W by Hallcrest Inc., are employed. A spatially-uniform constant-heat flux thermal boundary condition is implemented by a 25 μm thick Inconel foil, which is attached to the vertical heat transfer measurement surface. Covering the entire axial length and 90% of the channel height (18 cm out of 20 cm), the test plate is subjected to Joule heating from an *Agilent 6032A* DC power supply. The imposed surface heat flux q is calculated from supplied voltage and current $q = V \cdot I$.

For optimal TLC color-play brilliance and contrast, the thermochromic liquid crystals are deposited on a uniform underlying layer of matte black paint which exhibits a non-dazzling surface due to diffuse reflection. The test surface TLC response is observed via a Nikon D300S digital camera, placed at a 40° observation angle

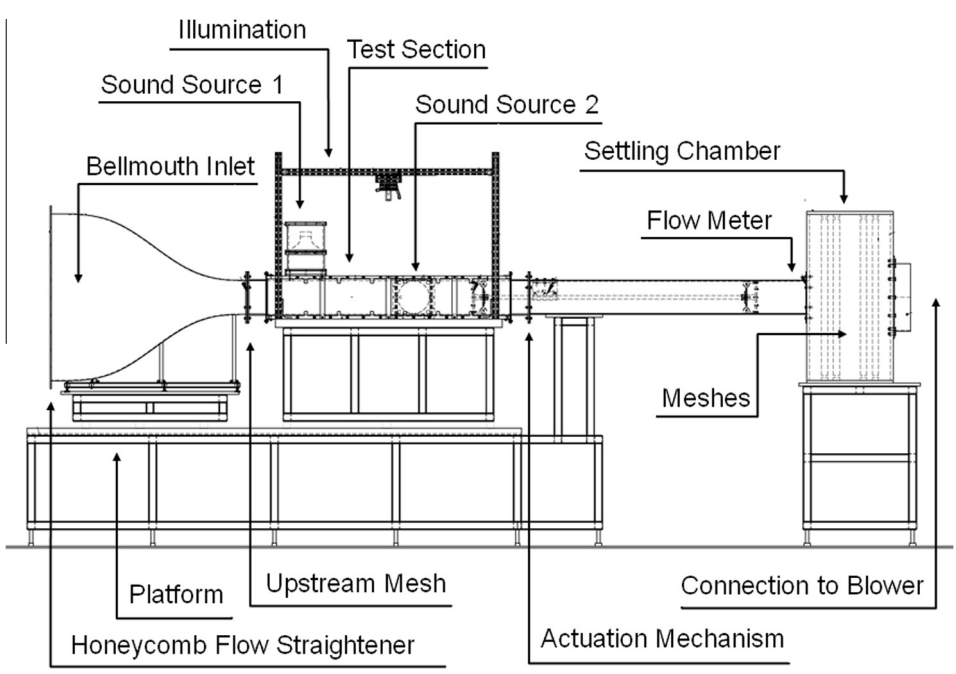

Fig. 2. Schematic of the experimental facility.

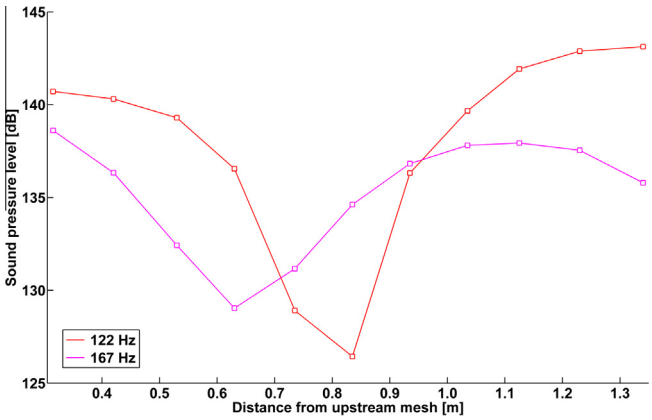

Fig. 3. Sound-pressure-level variation inside test section.

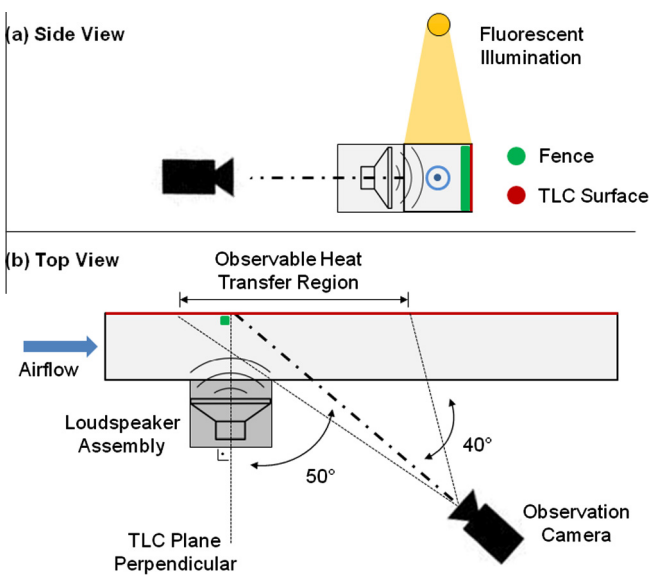

Fig. 4. Illustration of experimental configuration.

from the channel axis. A camera off-axis illumination configuration is used, ensuring minimum surface reflections, shadows and overcoming issues of non-uniformity. Illumination is provided by OSRAM type T8 L 36W fluorescent lights, mounted above the principal axis, irradiating at a 1 m vertical distance from the TLC surface, Fig. 4. The entire test section and observation camera are covered with a thick black cloth to prevent spurious background illumination sources.

2.4. TLC calibration and data reduction

During data acquisition, high-resolution images of the active TLC surface are captured in the RGB color space of the camera. To reduce a possible angular dependency due to camera-lighting off-axis arrangement, a background subtraction routine is utilized. RGB values of the unheated/inactivated TLC surface (background image) are sampled at the beginning of an experiment and subtracted from every subsequent measurement image. The effectiveness of this methodology was previously demonstrated [31].

In order to quantify the local surface temperature, RGB tristimulus color values are mapped into the HSI space:

$$H = 1/2\pi \cdot \tan^{-1}\left[\sqrt{3}\cdot(G-B)/(2R-G-B)\right] \quad (1)$$

The hue-angle color quantity can be uniquely correlated to temperature by a monotonously increasing, single valued and continuous function. This enables the unambiguous calculation of local surface temperature from the camera-recorded TLC response.

Hue-temperature calibration curve is established by an in-situ calibration at natural convection, using 4 T-type surface thermocouples located at the downstream end of the test plate. Arranged in a cross shaped configuration and enclosing a small TLC coated square (1×1 cm), the hue-angle value of exposed area is acquired and correlated with averaged thermocouple readings. The successively imposed temperature levels span the entire TLC color play bandwidth. Discrete data is fitted by a twice-differentiable, monotonically increasing 20 knot cubic spline. Details of TLC thermometry technique and the calibration procedure are given in [31].

Due to the inclined observation path, sampled images are subjected to significant perspective distortions. Each region of the image must therefore be mapped and projected separately onto a single plane via independent bicubic transformation, Fig. 5. Accordingly, due to the optical path, the magnification factor varies along the test plane; as an overall indicator, the averaged mean scale factor is calculated to be 12 pixels/mm.

Finally, after utilizing the calibration curves and converting acquired hue-angle distributions to the desired maps of surface temperatures, the raw temperature data is subjected to a series of median and Gaussian low pass filters.

2.4.1. Enhancement factor calculation

The local convective heat transfer coefficient is calculated from the (conduction losses-corrected) Inconel heat flux, the TLC-acquired surface temperature and the bulk temperature along the channel axis (linearly approximated from the inlet and exit section TC measurements):

$$h(x,y) = q/(T(x,y) - T_\infty(x)) \quad (2)$$

which is further non-dimensionalized by the channel hydraulic diameter based Nusselt Number:

$$\mathrm{Nu}_D(x,y) = h(x,y)\cdot D_h/k_{\mathrm{air}} \quad (3)$$

Sound-induced modification of convective heat transfer is quantified by the local enhancement factor EF, contrasting the Nusselt number in the presence and the absence of forcing:

$$EF = \mathrm{Nu}_{\mathrm{excited}}/\mathrm{Nu}_{\mathrm{unexcited}} \quad (4)$$

2.5. Uncertainty analysis

The measurement uncertainty is estimated according to the single sample method proposed in Ref. [32]. The overall uncertainty in wall temperature is determined by the uncertainty of thermocouple readings (±0.35 K), hue-angle contribution of the fixed broadband image noise (±0.25 K), the liquid crystals' angular dependency (±0.3 K) and deviation from the hue-temperature curve fit formulation (±0.2 K). This results in a combined wall temperature uncertainty of (±0.55 K). The major contributor to the heat flux uncertainty is the back face conduction loss, which yields deviations up to ±2.4%. Along with uncertainty on flow temperature, air thermal conductivity and hydraulic diameter measurement, the resulting nominal Nusselt number error is ±3.6%. The error associated with the enhancement factor, however, is a matter of measurement precision, and not necessarily accuracy. As a consequence, the EF uncertainty is determined in terms of repeatability and is estimated to be less than ±1.5%.

The total uncertainty in Reynolds number is in the order of 3.5%. This value represents an upper bound on measurement accuracy, as the experimentally determined mean deviation (precision)

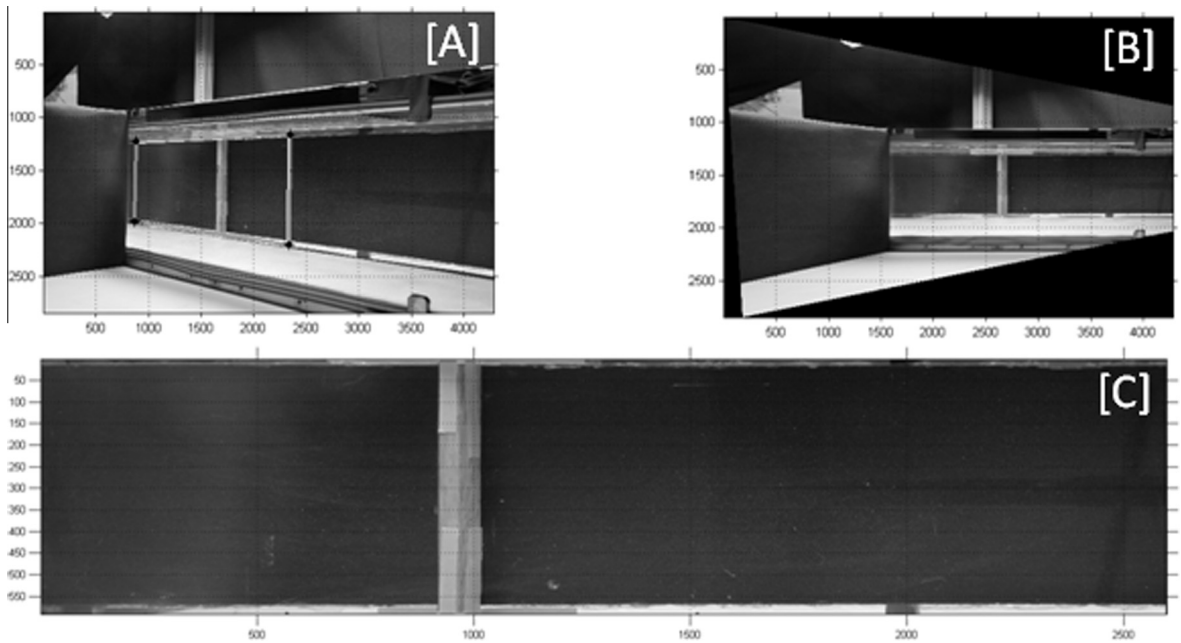

Fig. 5. Image perspective correction: A – raw form, B – projective transformation, C – cropping.

appears to be around 0.5%, adequate to ensure satisfactory repeatability.

3. Results

Measurements of convective heat transfer and steady pressure are conducted for a nominal Reynolds number of $Re_D = 134{,}000$ and $Re_H = 10{,}050$, based on channel hydraulic diameter (20 cm) and rib height (1.5 cm) respectively. The rib aspect ratio ($D_h/H = 13.3$), greater than 10, satisfies the two-dimensionality criterion of reattaching flows, defined for rearward-facing steps [33]. Therefore, the flow at the symmetry plane is considered to be unaffected by lateral wall influence.

3.1. Unexcited heat transfer distribution

For a region spanning 30 to 108 cm from inlet mesh, the unexcited baseline heat transfer distributions are portrayed in terms of the Nusselt number (Nu_D); referenced with respect to the fence downstream edge, this corresponds to $-20 < x/H < 32$, Fig. 6. As no heat transfer data is acquired on top and directly upstream of the rib (due to the blocked camera observation path), regions $-2.33 < x/H < 0$ are blanked out. Demonstrated to be in the vicinity of time-averaged flow reattachment x_R [5,34], the curve of streamwise maximum heat transfer (x_{max}) is indicated in grey and considered as the relevant indicator of steady skin friction reversal.

The characteristic aero-thermal features of the rib-roughened flow topology were previously discussed in detail for high blockage ratios (BR = 30%) and similar Reynolds number $Re_H = 12{,}000$ [6,35,36]. Examining the current Nu_D findings (for BR = 7.5% at $Re_H = 10{,}050$, as portrayed in Fig. 6), the upstream region $-19 < x/H < -2.33$ is characterized by the unperturbed boundary layer development over a flat plate prior to the influence of the rib obstacle. In this state, an overall gradual decrease in heat transfer is associated with boundary layer thickening at increasing development length from the inlet. Overall, towards the lateral wall $y/H \sim 3.3$, higher levels of heat transfer are observed, as a result of the corner wall vortices associated with the channel flow geometry.

Approaching the rib, due to the potential blockage effect, the flow separates from the surface and deviates around the rib obstacle. Owing to reduced cross-sectional area, it is locally accelerated and subsequently experiences an abrupt step change at the backward face of the rib. Confined by the flow reattachment line, an elongated recirculation bubble is formed. In current configuration, the separated flow region occupies a distance of approximately 8–10H.

As the most prominent flow feature, the flow reversal exerts large variations in heat transfer; in addition to forming a low momentum region, the entrainment of cool free stream fluid is prevented. Thus, the rib wake separation bubble imparts a global minimum in Nusselt number $Nu_D = 370$ at the immediate vicinity of the rib ($x/H \sim 0$), which is evident along the entire passage width.

Further downstream of the rib from $x/H \sim 1.5$, the Nusselt number begins to increase monotonously, as a consequence of the diminishing rib wake effects which allow cooler flow to be progressively entrained from the mainstream. At an increased axial position, this steep rise reaches a global maximum ($Nu_D \sim 580$) in the vicinity of the reattachment point. This is associated with the strong impingement of the separated free shear layer on the bounding wall, subjecting the heated surface to high-momentum fluid with lower temperature.

Although the aerodynamic reattachment point (x_R) and maximum streamwise heat transfer position (x_{max}) do not universally coincide for all separated flows, x_{max} is considered as the relevant indicator of skin friction reversal point [5,34]. Towards the sidewalls, the local heat transfer maxima levels increase, the positions of which are observed slightly further upstream, Fig. 6. This curved spanwise distribution and laterally increasing heat transfer are attributed to the aerodynamic wall effects and rolled up corner vortices being advected over the rib from the upstream separation point [6,37]. Beyond the reattachment point, $x/H > 10$, the heat transfer decreases monotonically in the streamwise direction with the redeveloping thermal boundary layer and eventually re-approaches its initial unperturbed boundary layer state, $x/H > 27$.

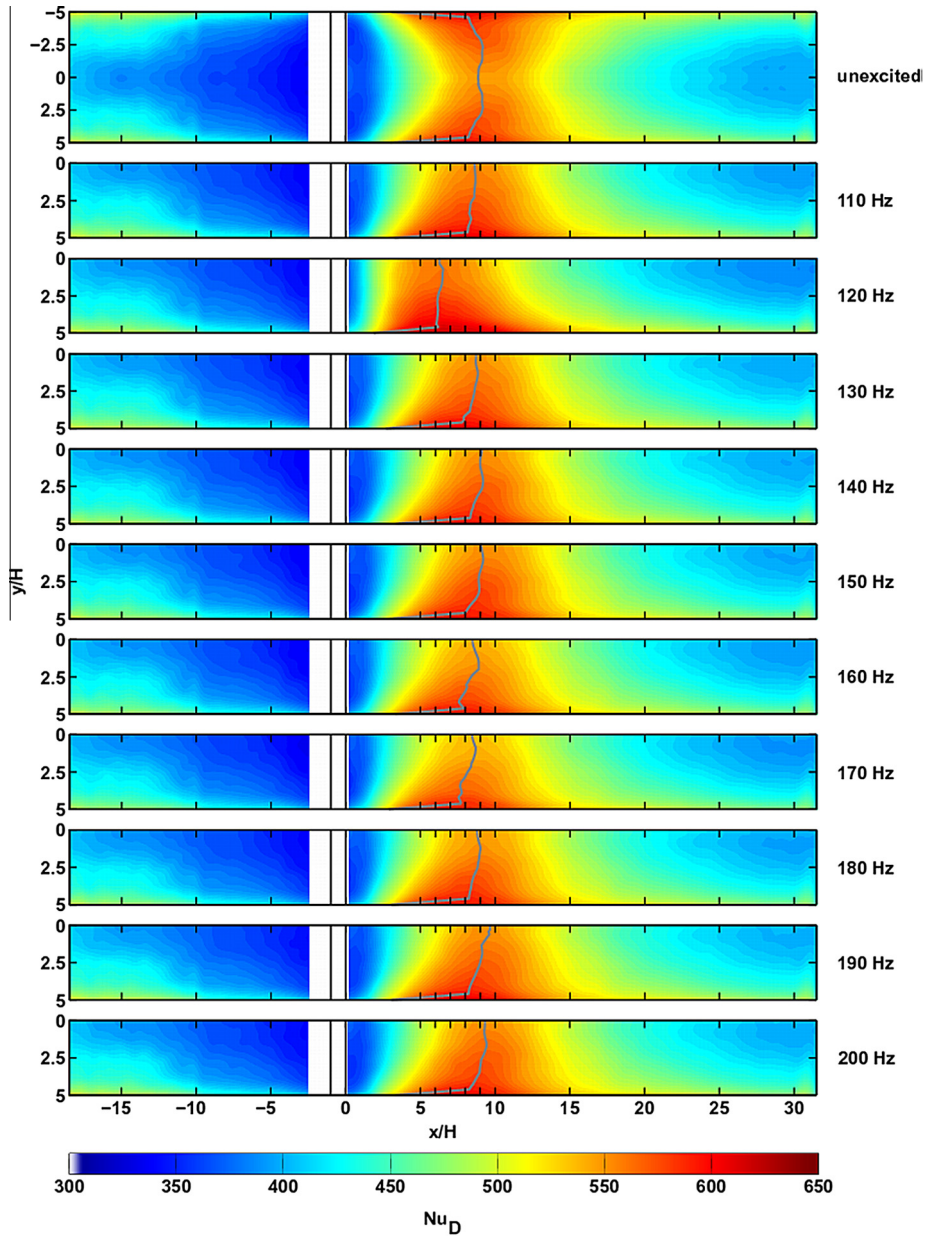

Fig. 6. Nusselt number distributions – frequency variation.

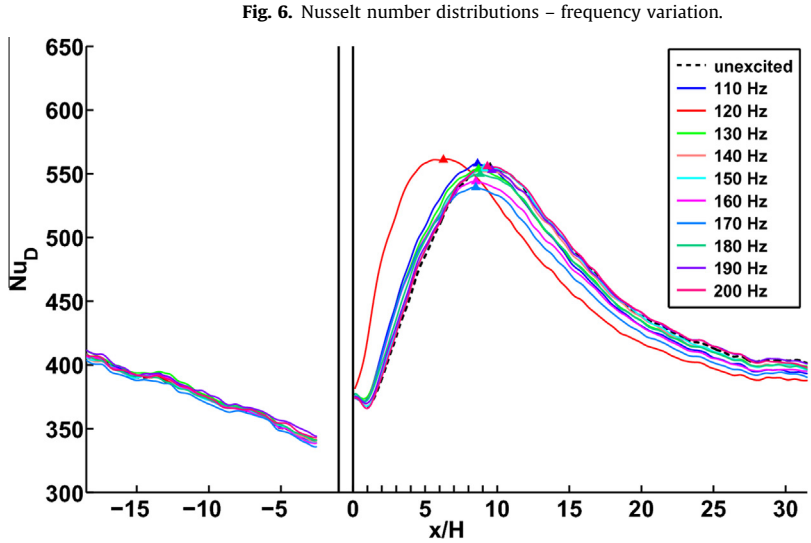

Fig. 7. Centerline Nusselt Number – Frequency Variation.

3.2. Excitation frequency variation

Subsequently, the baseline flow is acoustically excited with 110–200 Hz harmonic forcing (corresponding to Strouhal number range $\mathrm{St} = f \cdot H/U = 0.16 - 0.29$) at 131 dB SPL, Table 1. In comparison, for mean flow velocities up to 10 m/s, the background noise absent of excitation is measured to be less than 80 dB. Within the excitation range, forcing frequencies of 120 Hz and 170 Hz are conducive to standing wave formation. Surface microphone measurements indicated that SPL amplitudes of both acoustic resonances are of same order of magnitude. Despite some differences in the resonance mode shapes, the pressure antinode locations are similar -roughly 18 step heights upstream of the rib (30 cm from the inlet mesh). The other forcing frequencies are mere traveling wave excitations. The 110–200 Hz excitation range falls within the wide conducive traveling wave forcing reported in various literature, St = 0.1–0.7 [3,4,38,39]. Although initially a much broader frequency range was considered, no noticeable impact is observed beyond the presented frequencies.

3.2.1. Heat transfer distributions

Demonstrating the convective heat transfer implications of harmonic excitation for various frequencies in the 110–200 Hz range, Fig. 6 presents detailed distributions of local Nusselt number (Nu_D) over a domain spanning 20 step heights upstream and 32 step heights downstream of the rib. The line of streamwise maximum in heat transfer, x_{max}, is indicated by the thin grey line. In addition, centerline heat transfer along the channel axis is presented in Fig. 7 for each frequency, where an asterisk indicates the point of the local maximum.

Upstream of the fence ($x/H < -2.33$), identical heat transfer distributions reveal the oncoming flat plate boundary layer flow to be entirely unaffected by forcing in the 110–200 Hz range, Fig. 6 and Fig. 7. Overlapping excited and unexcited Nu_D developments reflect the imperviousness of the attached flow boundary layer to both traveling and standing wave forcing. For the longitudinal standing waves, literature on the pipe flow convection has demonstrated that M_∞/M_o^2 is the relevant descriptor of the flow phenomena, and threshold resonance disturbance to produce an observable change is less than 63 [20–24]. For this configuration, the value is in the order of 300, and hence, the acoustic energy introduced is not sufficient to create local aero-thermal flow features on the attached boundary layer.

In contrast, the heat transfer surface associated with the reattaching flow downstream of the rib is more prone to discrete frequency dependent response, Fig. 6 and Fig. 7. For $x/H > 0$, the changes are more prominently depicted on the lateral distribution of the streamwise maximum heat transfer curve (x_{max}). Comparing the different forcing frequencies, most traveling sound waves (at 110, 130, 140, 150, 180, 190, 200 Hz) do not seem to be conducive towards noticeable manipulation of the fence wake heat transfer, as the distribution of the reattachment curve is not significantly altered in Fig. 6. Moreover, with respect to the baseline case, the excitation imparts minimal changes in the vicinity of the reattachment curve, $x/H \sim 9$, where a minor upstream shift in maximum heat transfer point (within $\Delta x_{max}/H \sim 0.5$) is visible, Fig. 7. The peak level of Nu_D remains unchanged, followed by a slight drop in redeveloping flow heat transfer levels, $x/H > 9$. This reduction is possibly associated with the viscous dissipation of the periodic traveling wave perturbation, and the resultant local decrease in fluid to wall temperature difference.

In contrast to minimal heat transfer variation in the presence of traveling waves, when the flow over a fence is subjected to acoustic resonance forcing at 120 Hz, the induced longitudinal standing sound wave exerts a notable influence on the aero-thermal wake flow field. While the local minimum heat transfer remains in the vicinity of the rib back face, the steep streamwise gradient in the separation region appears to be augmented as a consequence of the sound excitation, Fig. 7. A small increase in the peak heat transfer level (around 5%) is observed. The extent of the recirculation bubble is significantly reduced under the influence of acoustic excitation, shifting the location of centerline maximum heat transfer from $x_{max}/H = 9.5$ to $x_{max}/H = 6$. Towards the lateral walls at $y/H \geqslant 3.33$, a similar observation can be made, moving x_{max}/H from 8.5 to 6, Fig. 6. Therefore, while the line of unexcited flow reattachment exhibits a curved shape in the spanwise direction, it becomes flattened in the presence of forcing – evidenced by uniform $x_{max}/H = 6$ in Fig. 6. The local heat transfer benefit associated with this excitation is quantified in the form of enhancement factor. While the maximum of 25% enhancement is observed around the centerline at $x/H \sim 1.5$ and $|y/H| < 2.5$, it reduces gradually in both the streamwise and lateral directions. As the excited re-attached flow starts to develop at an earlier streamwise position ($x/H \sim 6$), it results in thickening of the thermal boundary layer. Therefore, downstream of $x/H \sim 8$, the local heat transfer level of the re-developing attached flow region appears to be lower with respect to the unexcited case. The enhancement factor decays to a global minimum of ~0.9 at $x/H = 12.5$. Far away from the obstacle, the resonance induced effects gradually diminish.

Despite similar SPL amplitudes of both acoustic resonances, the standing sound wave at 170 Hz imparts only limited changes on the heat transfer distribution, Fig. 6. The line representing the streamwise maximum in heat transfer distribution appears slightly more corrugated than in the unexcited case, and is accompanied by a slight upstream shift of 0.5 order. Moreover, at any streamwise location downstream of the fence – including the reattachment associated peak region, a broad 5% decrease in heat transfer is observed, Fig. 7. Clearly, the combined effect is detrimental to local and global heat exchange. Interestingly, although the 160 Hz excitation is initially categorized as a traveling wave, the heat transfer signature depicted is similar to the 170 Hz resonance forcing. It is perhaps too close to the eigenfrequency band conducive to the generation of a standing wave.

3.2.2. Static pressure distributions

In order to supplement prior heat transfer observations, as an aerodynamic indicator, the forcing impact on the separated and reattaching wake flow field is analyzed by wall static pressure measurements. For 70–270 Hz range frequencies, Fig. 8 portrays the duct centerline pressure development at 6 locations over a distance of 30 rib heights. Normalized by the dynamic pressure head, $(p\text{-}p_{\mathrm{ref}})/(0.5\rho U^2)$, the values are reported in reference to the fence upstream port at $x/H = -10$. With respect to the baseline case, traveling sound wave excitation below 100 Hz and above

Table 1
Excitation frequency dependence.

Freq. [Hz]	110	120	130	140	150	160	170	180	190	200
Resonance	–	✓	–	–	–	–	✓	–	–	–
Strouhal [–]	0.16	0.17	0.19	0.20	0.22	0.23	0.25	0.26	0.27	0.29
SPL [dB]	131	131	131	131	131	131	131	131	131	131

200 Hz induces no modification of the wall pressure development. This rationalizes the selection of the 100–200 Hz range for the presented heat transfer investigation.

Even within this frequency range, upstream of the rib has no static pressure variation for any excitation frequency, Fig. 8. Downstream of the rib, pure traveling sound waves 100, 140, 150, 180, 190, 200 Hz result in negligible change within the separation region, for which the trends closely coincide with the unexcited baseline curve. In contrast to such mere minimal variations, the standing waves at 120 and 170 Hz clearly depict faster initial pressure recovery, evidenced by the elevated pressure levels at static port of $x/H \sim 6.5$. It is noteworthy that the excitation at 240 Hz, the first overtone of the 120 Hz base eigenfrequency, does not promote an aerodynamic response.

Similarly, curves of traveling wave forcing at 110, 130, 160 Hz reflect small yet quantifiable increases in static wall pressure, which are most likely attributed to excitation of the neighboring resonance frequencies around 120 and 170 Hz. In order to verify this conjecture, measurements are carried out with 1 Hz excitation increment around both resonances, 120 ± 10 Hz and 170 ± 10 Hz, Fig. 9 and Fig. 10 respectively. The most pronounced changes occur at the exact eigenfrequency excitations of 122 Hz and 167 Hz. In the neighboring frequencies, evidenced by the continuous gradual change which progressively vanishes, favorable forcing associated with standing wave interferences is determined to be partially excitable by slightly off-resonance conditions. This corroborates the assumption that static pressure variations at 110, 130, and 160 Hz excitations are a result of their close proximity to respective resonance conditions. However, no heat transfer ramifications were observed at these conditions.

Therefore, contrasting the time-averaged static pressure signature of pure traveling and standing waves, higher spatial resolution data is acquired at selected excitation conditions of 100, 122, 167, 200 Hz, Fig. 11. The slight change in resonance forcing conditions (122 instead of 120 Hz, and 167 instead of 170 Hz) are to provide a fair comparison between both standing wave conditions.

For all conditions (excited and unexcited), the region upstream of the perturbator ($-8 < x/H < -1$) portrays the unaffected gradual pressure rise, which is associated with the potential blockage effect of the rib. Furthermore, consistent with prior findings for heat transfer, the acoustic excitation does not impose any changes to the local pressure field, supporting the observation that the oncoming upstream boundary layer is unaffected by acoustic forcing. Downstream of the fence, $0 < x/H < 13.5$, standing wave conditions in 122 Hz and 167 Hz are characterized by an upstream shift of streamwise pressure trends, indicating an faster static pressure recovery within the recirculation zone. Moreover, occurring at $x/H \sim 3.5$ for the unexcited case, the local pressure minima shifts upstream. This is more prominent in the 122 Hz excitation, for which the recovery is initiated as early as $x/H \sim 1$. On the other hand, the pressure minima at 167 Hz resonance shifts less than a rib height. Further downstream of the rib in the vicinity of flow reattachment ($x/H \sim 9$), the steepened gradients beyond the global pressure minima are seen to level off and gradually converge to an identical static pressure level at around $x/H \approx 12$–13. As indicated by the invariant downstream pressure level for the flow over the fence, the pressure drop penalty incurred remains unchanged. With a constant D'arcy friction factor of around $f = 0.14$, the total pressure loss is inferred to remain constant.

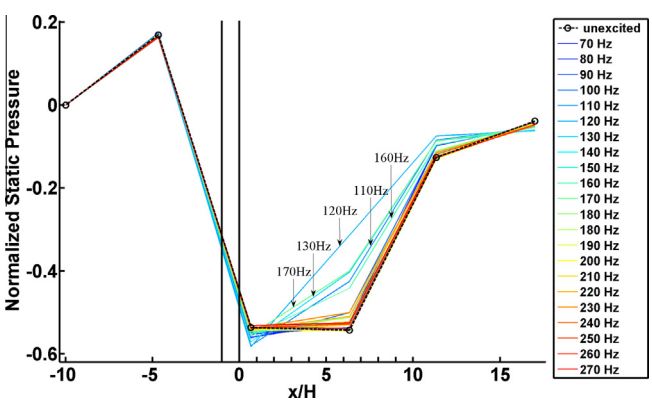

Fig. 8. Centerline static pressure – frequency range 70–270 Hz.

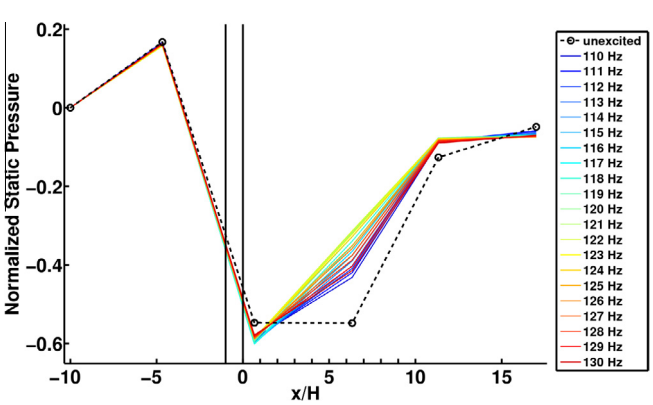

Fig. 9. Centerline static pressure – around 120 Hz resonance.

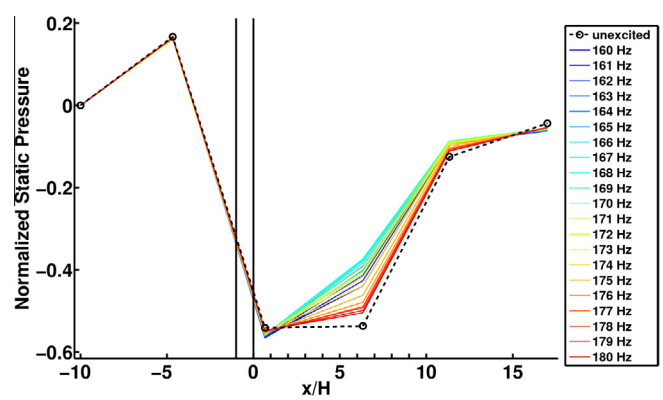

Fig. 10. Centerline static pressure – around 170 Hz resonance.

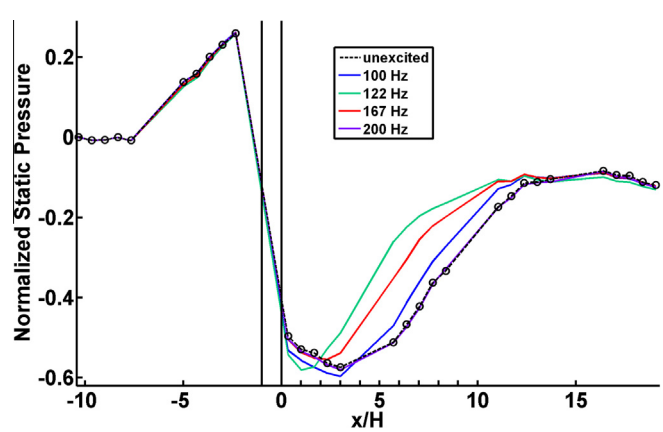

Fig. 11. Centerline static pressure – high resolution.

Regarding the invariance of static pressure downstream of the separation region both absent and present of forcing, it can be deduced that the associated aerodynamic loss mechanism is unaffected despite prominent excitation induced changes in the reattachment region. As it is primarily the recirculation bubble which causes the pressure drop, the associated recirculation (integral vorticity) can be hypothesized to remain constant. For the conducive excitation, the slightly lower initial pressure at the rib back face, along with the earlier recovery, could be indicative of a smaller vortex of greater vorticity, rotating at a higher rate, at the immediate downstream of the rib. Consistent with the findings, prior flow control literature in a different phenomenological setting (periodical oscillations of an upstream jet) demonstrated that the reduction in steady aerodynamic reattachment length was accompanied by invariant total pressure drop, an intensification of turbulent fluctuations, increased turbulent kinetic energy, as well as more rapidly growing and higher vorticity thickness [4,19].

In contrast to the resonance effects, the pure traveling wave excitations at 100 and 200 Hz correspond to negligible changes in the static pressure signature, which attests to the unreceptiveness of the time-averaged pressure field to this kind of forcing. This is in contradiction with previous aerodynamic work on the abruptly separated flow control subject. Perhaps the disparity is associated with the presently employed global excitation with a very small local perturbation requirement, in contrast to the previously employed local forcing via jets or mechanical flaps with much larger and concentrated energy input.

Hence, it is observed that the 122 Hz resonance has significant aerodynamic and thermal impact. On the other hand, the standing wave forcing at 167 Hz results in a slight pressure variation but it is not conducive to heat transfer modifications. These findings can be contrasted with prior aerodynamic literature, despite vast differences in type and frequency of excitation as found in Ref. [19] (local oscillating jet at St = 0.05 on the same wall as the rib). It was observed that although the time-accurate flow reattachment point remains invariant, the conducive excitations reduced the time-averaged separation length. In the scope of the current article, considering static pressure as an indicator of the time-mean flow field, temporally averaged aero-thermal fields may not necessarily correlate in the presence of highly unsteady instantaneous flow features. Therefore, the changes in the time-averaged pressure field do not directly translate into wall heat transfer variations.

Table 2
Strouhal number dependence.

Configuration	Freq. [Hz]	H [cm]	Strouhal [–]	Re_D
A	120	1.5	0.22	101,000
	90		0.17	
B	120	1.5	0.17	134,000
	90		0.13	
C	120	2	0.22	134,000
	90		0.17	

3.3. Strouhal number dependence

The source frequency variation experiments revealed that the largest steady aerodynamic impact, and the only case with significant heat transfer ramifications is associated with 120 Hz excitation. Accordingly, it is yet to be clarified whether this effectiveness is attributed to the existence of a sharp Strouhal number conducive towards wake flow modification via periodic traveling wave oscillations, or if the observed phenomenon is associated with the presence of the acoustic resonance mode.

A concise aerodynamic experiment is designed to cast light on this mechanism. For the same Strouhal number, by contrasting wall pressure implications of 120 Hz resonant forcing to the effects of 90 Hz pure traveling wave excitation, the role of forcing frequency and excitation type (traveling/standing waves) are decoupled. As indicated in Table 2, the three test configurations (A, B, C) are associated with different fence height (1.5 cm, 2 cm) and Reynolds number (101,000, 134,000) combinations. The 120 Hz forcing of configuration B and the 90 Hz excitation of configurations A and C (which are characterized with a lower flow velocity and larger rib respectively) all result in St = 0.17. Along the same lines, the 120 Hz excitation of configurations A and C yield St = 0.22.

Fig. 12 contrasts the normalized pressure distributions for each test condition with forcing to its correspondent unexcited baseline trends. In the unexcited cases, it can be seen that the wake flow signature retains similarity and different pressure levels are an artifact of successively increased pressure drop from configuration A (low Re, nominal H), to B (nominal Re, nominal H), and to C (nominal Re, high H).

Comparing the level of receptiveness, subjected to the 90 and 120 Hz excitation frequencies under different flow and geometric conditions, the earlier pressure recovery is seen to be limited to 120 Hz resonance condition forcing and it is independent of the Strouhal number. In contrast, for the St range of 0.13–0.17, traveling wave excitation at 90 Hz never exhibits any aerodynamic impact. Moreover, cases A and C depict the evident aerodynamic effects of 120 Hz excitation at a greater Strouhal number, St = 0.22.

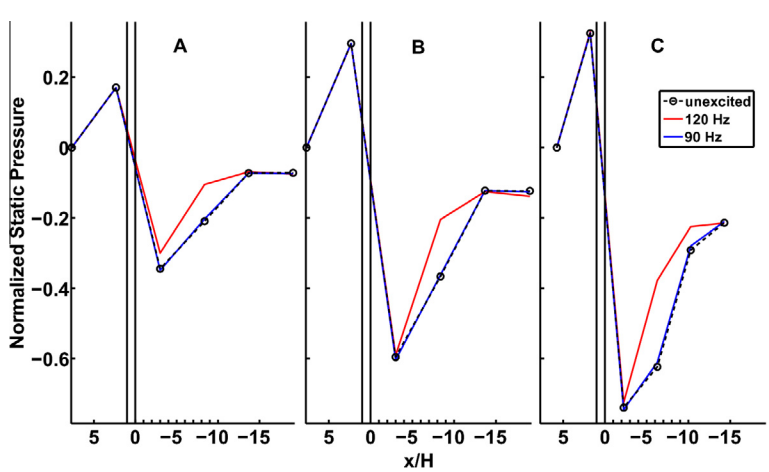

Fig. 12. Strouhal number variation: A – Re = 101,000, H = 1.5 cm; B – Re = 134,000, H = 1.5 cm; C – Re = 134,000, H = 2 cm.

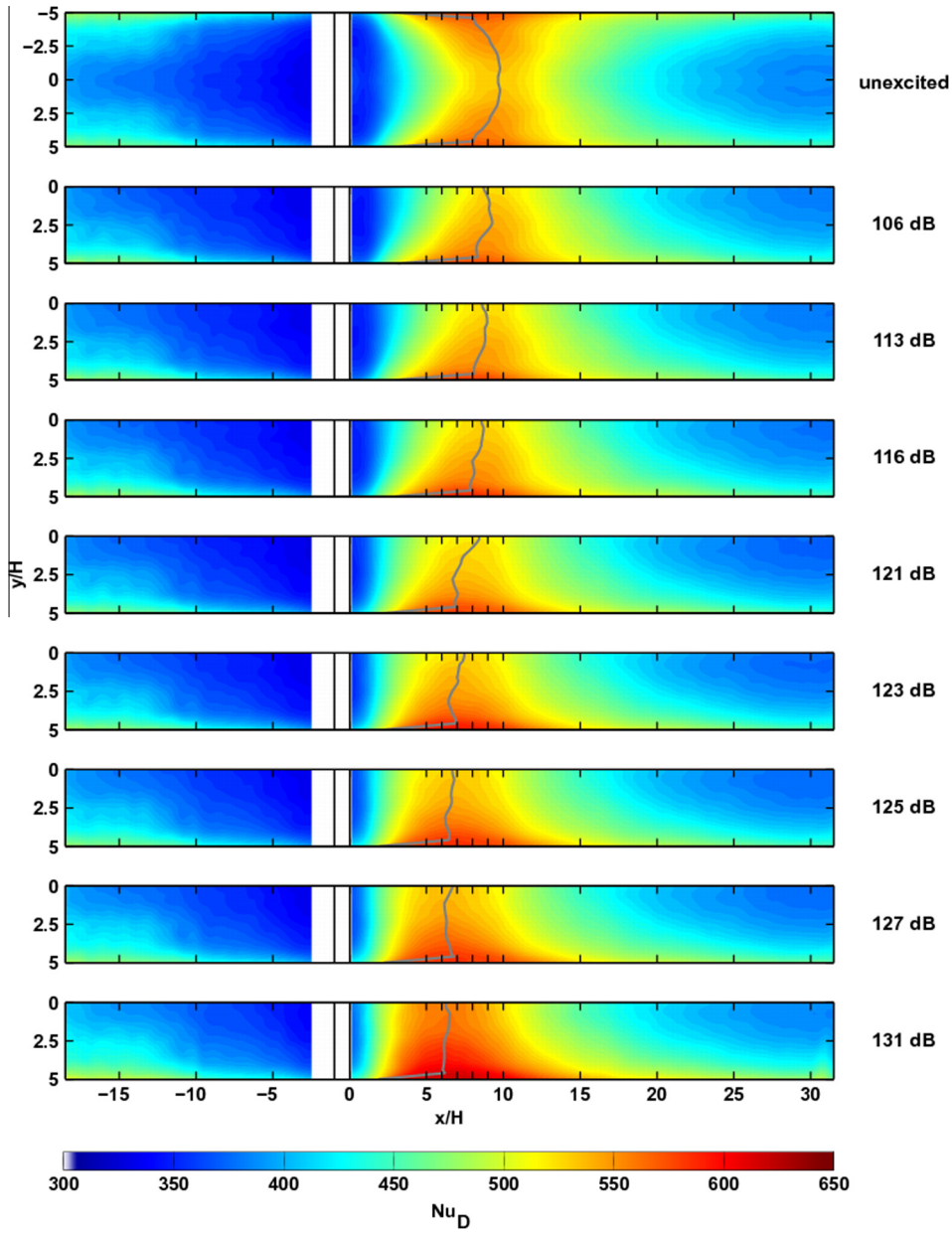

Fig. 13. Nusselt number distribution – 120 Hz SPL variation.

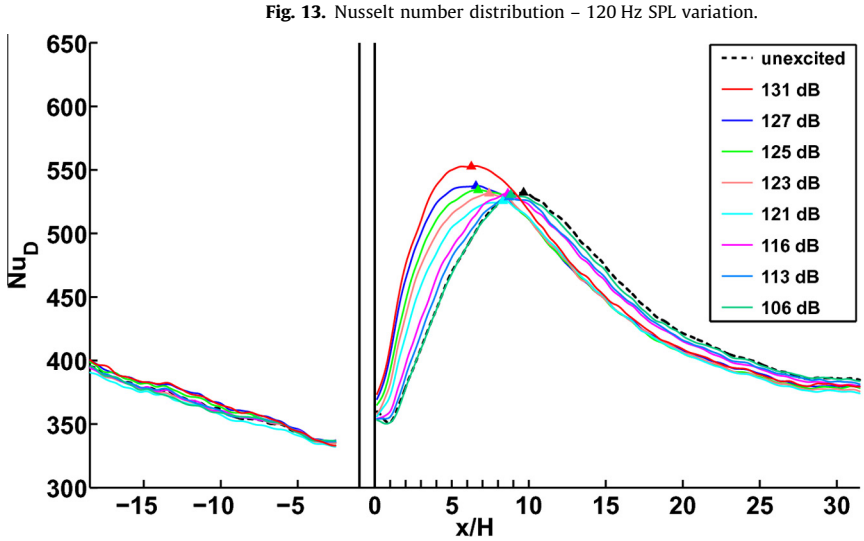

Fig. 14. Centerline Nusselt number – 120 Hz SPL variation.

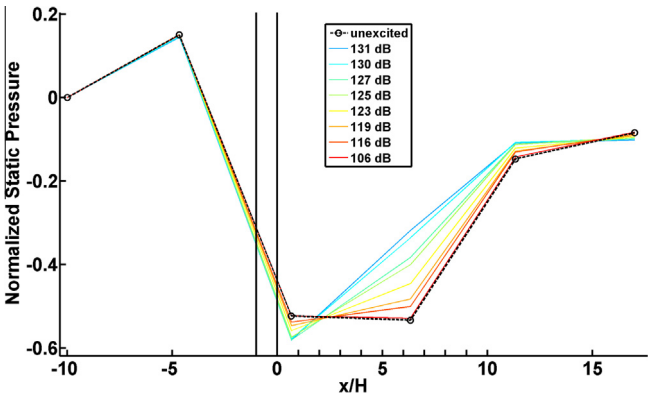

Fig. 15. Centerline static pressure – 120 Hz SPL variation.

In the scope of conditions observed within this study, evidenced by the parametric variation which decouples the role of absolute source frequency from Strouhal number, achieving a notable aero-thermal impact on rib roughened flow is only possible via standing sound waves which reside in a St range that includes 0.17–0.22. Beyond this region, as observed for the 170 Hz resonance forcing at around St = 0.26, adverse aero-thermal ramifications may exist, resulting in lower heat transfer and an invariant flow reattachment length.

3.4. Excitation amplitude variation

Prior observations indicate that acoustic excitation conducive towards notable heat transfer modulation is associated with resonance at a favorable Strouhal number. The remaining question is the dependence of aero-thermal implications on the excitation amplitude (SPL). Addressing this aspect, for the 120 Hz effective resonance excitation under nominal conditions, the sound pressure level is incrementally varied from 103 to 131 dB. The corresponding heat transfer distributions and Nu_D centerline trends are charted in Fig. 13 and Fig. 14, respectively. Furthermore, centerline static pressure development is presented in Fig. 15.

For the source SPL range of 103–116 dB, the location of the stream-wise peak in heat transfer remains unchanged towards the sidewalls $|y/H| > 2.5$ and recedes minimally ($\Delta x_{max} \sim 0.5H$) in the vicinity of the centerline, Fig. 13. Contrasting the heat transfer development at $y/H = 0$, Fig. 14, it can be seen that these conditions are not conducive to heat transfer modification. Comparing the effects of these excitation amplitudes on wall static pressure, the resonant forcing below 121 dB source level is seen to induce minimal changes – the same order as the traveling sound waves prior studied.

At around 121 dB source SPL and beyond, notable aero-thermal impact of 120 Hz resonance excitation is indicated by an evident gradual upstream shift of the Nu_D curve, Fig. 13. Eventual lateral straightening of the maximum heat transfer curves induce transition of the initially parabolic reattachment line to a near flat shape. In the course of SPL increase from 121 to 131 dB, the maximum heat transfer location on the centerline moves from its initial position at $x_{max}/H = 9$ to 8.5, 7.5, 6.5, and finally to 6 (Fig. 14). Simultaneously, the peak level Nu_{max} exhibits a limited rise. Negligible below 127 dB, the augmentation is less than 5% at the highest SPL of 131 dB. Nevertheless, in the $x/H = 3$–4 range, the pronounced steepening of the streamwise heat transfer gradient prior to reattachment induces locally enhanced Nu_D with respect to the unexcited baseline case – about 12.5%, 16.5%, 18.5%, 23%, 25% at 121 dB, 123 dB, 125 dB, 127 dB, and 131 dB respectively. Indicated by continuously rising levels of pressure recovery within the separation region (Fig. 15), the wall static pressure data confirms the steadily increasing effectiveness of the excitation beyond 121 dB. On the other hand in Fig. 14, indicated by the collapse of heat transfer curves onto the same streamwise slope at $x/H > 9$, locally 8% lowered Nu_D downstream of reattachment remains roughly at the same level independent of forcing amplitude.

In brief, exciting the 120 Hz resonance with a source SPL beyond 121 dB exhibits clear aerodynamic and heat transfer effects, which are significantly beyond the effectiveness of traveling wave forcing at much higher SPL of 131 dB. Below this 121 dB excitation threshold, no impact is noticeable. Relating this separated flow resonance sound pressure level to a non-dimensional quantity typically defined for attached pipe flow, it is observed that $M_\infty/M_o^2 < 3300$ is the condition to produce significant modification in the re-attachment region. Moreover, the aero-thermal impact becomes more pronounced with increasing excitation level. Overall, a maximum amplitude saturation level, for which the beneficial impact stagnates, is not observed.

4. Summary and conclusions

Within the scope of this article, the effects of acoustic excitations on turbulent convective heat transfer and separated flow reattachment are studied in the presence of a squared isolated fence obstacle (with 7.5% passage blockage ratio) at a channel Reynolds number of 134,000. In order to demonstrate and quantify the sensitivity of acoustically coupled surface heat transfer modulation to various excitation parameters, Nusselt number distributions and centerline static wall pressure developments are acquired for different forcing frequencies and amplitudes, 70–270 Hz (St = 0.1–0.38) and 103–131 dB SPL respectively. Frequencies conducive to longitudinal standing sound waves generation are identified as ~120 Hz (St = 0.17) and ~170 Hz (St = 0.26). When excited by acoustic forcing, the resulting mode shape patterns are experimentally verified via surface microphone measurements.

For all conditions, upstream of the fence ($x/H < -2.33$), unchanged heat transfer and static pressure distributions reveal the oncoming flat plate boundary layer flow to be entirely unaffected by the forcing. On the contrary, at conducive conditions, a pronounced impact on the rib downstream separation region is ascertained. In the presence of the 120 Hz acoustic resonance excitation, which corresponds to St = 0.17, local heat transfer enhancement and earlier pressure recovery is observed on the reattaching flow. A strong diminishing influence on the recirculation bubble is manifested as an upstream shift of the maximum heat transfer line by up to $\Delta x_{max} = 3.5H$ or 37%. This is most prominent at the channel centerline. Therefore, exhibiting a curved shape absent of forcing, the flow reattachment line under excitation is flattened significantly in the lateral direction. Retaining an overall self-similar pattern, the streamwise bell shaped Nusselt curve moves upstream with a slight increase in maximum heat transfer of ~5%. Contrasting the associated local heat transfer distribution with the unexcited case, local enhancement of up to 25% is observed; meanwhile, a slight heat transfer reduction of 8% occurs further downstream. Complementary wall static pressure measurements clearly reflect the upstream shift of the time-averaged reattachment region, where a steeper local static pressure recovery is observed. Further downstream, the static pressure level remains invariant, such that the integral pressure drop penalty associated with the rib flow is entirely unchanged by the resonance forcing. Thence, the associated aerodynamic loss mechanism is inferred to be unaffected.

Indicating that forcing effectiveness can vary between different conditions, the other longitudinal resonance at 170 Hz eigenfre-

quency (St = 0.26) portrays slightly detrimental influence on heat transfer, accompanied by limited aerodynamic impact. In the frequency range investigated, even the highest SPL of the traveling wave excitations are not capable of manipulating the aero-thermal distributions downstream of the fence.

For the 90 Hz traveling wave and 120 Hz standing wave excitations, the role of absolute source frequency is decoupled from Strouhal number by varying the rib height and the Reynolds number. Based on wall static pressure distributions, forcing effectiveness is seen to hinge on the resonance condition. While the St = 0.17 excitation created by a standing wave achieves notable aero-thermal influence on rib roughened flow, matching the reduced frequency by a traveling wave does not produce any impact. It can be deduced that favorable conditions towards manipulating the separated shear layer, and the subsequent heat transfer modulation, are associated with standing sound waves within a favorable Strouhal range which includes St = 0.17–0.22.

At the conducive excitation conditions, the SPL dependence of the aero-thermal effect is analyzed. For significant impact on the re-attachment region, a minimum SPL threshold at around 121 dB is required – this corresponds to non-dimensional criteria of $M_\infty/M_o^2 < 3300$. Beyond the threshold amplitude, the aero-thermal influence increases monotonously with augmented SPL.

Conflict of interest

None declared.

Acknowledgements

The authors acknowledge the financial support of Technion-IIT, Minerva Research Center (Max Planck Society Contract AZ5746940764), Israel Science Foundation (Individual Grant #1752/15) and L. Kraus Research Fund towards initialization of this work. Furthermore, the scholarships which are utilized towards accommodation of Mr. Claudio Selcan in Israel, provided by the Heinrich Hertz-Stiftung (Ministry of Innovation, Science and Research of North Rhine-Westphalia), and Erich Becker-Stiftung (Fraport AG), are greatly appreciated.

References

[1] E.J. Rice, K.B.M.Q. Zaman, Control of shear flows by artificial excitation, NASA Technical Memorandum, NASA, Cleveland, OH, USA, 1987.
[2] D. Greenblatt, I.J. Wygnanski, The control of flow separation by periodic excitation, Prog. Aerosp. Sci. 36 (2000) 487–545.
[3] F.W. Roos, J.T. Kegelman, Control of coherent structures in reattaching laminar and turbulent shear layers, AIAA J. 24 (12) (1986) 1956–1963.
[4] S. Bhattacharjee, B. Scheelke, T.R. Troutt, Modification of vortex interactions in a reattaching separated flow, AIAA J. 24 (4) (1986) 623–629.
[5] E.M. Sparrow, S.S. Kang, W. Chuck, Relation between the points of flow reattachment and maximum heat transfer for regions of flow separation, Int. J. Heat Mass Transfer 30 (7) (1987) 1237–1246.
[6] L. Casarsa, T. Arts, Experimental investigation of the aerothermal performance of a high blockage rib-roughened cooling channel, ASME J. Turbomach. 127 (3) (2005) 580–588.
[7] C.M. Ho, P. Huerre, Perturbed free shear layers, Annu. Rev. Fluid Mech. 16 (1984) 365–424.
[8] F.K. Browand, T.R. Troutt, A note on spanwise structure in the two-dimensional mixing layer, J. Fluid Mech. 97 (1980) 771–781.
[9] C.M. Ho, L.S. Huang, Subharmonic and vortex merging in mixing layers, J. Fluid Mech. 119 (1982) 443–473.
[10] G.L. Brown, A. Roshko, On density effects and large structure in turbulent mixing layers, J. Fluid Mech. 64 (4) (1974) 775–816.
[11] C.D. Winant, F.K. Browand, Vortex pairing: the mechanism of turbulent mixing layer growth at moderate reynolds number, J. Fluid Mech. 63 (1974) 237–256.
[12] F.K. Browand, T.R. Troutt, The turbulent mixing layer: geometry of large vortices, J. Fluid Mech. 158 (1985) 489–509.
[13] T.R. Troutt, B. Scheelke, T.R. Norman, Organized structures in a reattaching separating flow field, J. Fluid Mech. 143 (1984) 413–427.
[14] J.K. Eaton, J.P. Johnston, A review of research on subsonic turbulent flow reattachment, AIAA J. 19 (9) (1981) 1093–1100.
[15] C. Chandrsuda, P. Bradshaw, Turbulence structure of a reattaching mixing layer, J. Fluid Mech. 110 (1981) 171–194.
[16] J. Kim, S.J. Kline, J.P. Johnston, Investigation of reattaching turbulent shear layer: flow over a backward-facing step, ASME J. Fluids Eng. 102 (1980) 302–308.
[17] D. Oster, I.J. Wygnanski, The forced mixing layer between parallel streams, J. Fluid Mech. 123 (1982) 91–130.
[18] F.K. Browand, B.O. Litago, Growth of the two-dimensional mixing layer from a turbulent and non-turbulent boundary layer, Phys. Fluids 22 (6) (1979) 1011–1019.
[19] H.A. Siller, H.H. Fernholz, Manipulation of the reverse-flow region downstream of a fence by spanwise vortices, Eur. J. Mech. B/Fluids 26 (2007) 236–257.
[20] K.R. Purdy, T.W. Jackson, C.W. Gorton, Viscous fluid flow under the influence of a resonant acoustic field, ASME J. Heat Transfer 86 (1964) 97–106.
[21] K.R. Purdy, T.W. Jackson, D.A. Willoughby, H.G. Keith, C.E. Willbanks, The Effect of a Resonant Acoustic Field on Laminar Flow in a Circular Tube, in ARL Report No. ARL65-96. 1965.
[22] T.W. Jackson, K.R. Purdy, H.G. Keith, R.S. Rudland, Investigations of the Effect of Acoustic Vibrations on Convective Heat Transfer, in ARL Report No. ARL-65-97. 1965.
[23] P. Merkli, H. Thomann, Thermoacoustic effects in a resonance tube, J. Fluid Mech. 70 (1) (1975) 161–177.
[24] T.W. Jackson, C.C. Oliver, I. Eastwood, The effects of resonant vibrations on heat transfer at high reynolds numbers, Georgia Institute of Technology, Atlanta, Georgia, USA, 1961.
[25] T.W. Jackson, W.B. Harrison, W.C. Boteler, Free convection, forced convection, and acoustic vibrations in a constant temperature vertical tube, ASME J. Heat Transfer 81 (1959) 68–74.
[26] R. Lemich, C.K. Hwu, The Effect of Acoustic Vibration on Forced Convective Heat Transfer, Am. Inst. Chem. Eng. (AIChE) J. 7 (1961) 102–106.
[27] K.K. Ahuja, R.R. Whipkey, G.S. Jones, Control of Turbulent Boundary Layer Flows by Sound. AIAA paper, 83–0726, 1983.
[28] K.K. Ahuja, R.H. Burrin, Control of Flow Separation by Sound. AIAA paper, 84-2298, 1984.
[29] K.B.M.Q. Zaman, A. Bar-Sever, S.M. Mangalam, Effect of acoustic excitation on the flow over a low-re airfoil, J. Fluid Mech. 182 (1987) 127–148.
[30] J.H. Bell, R.D. Mehta, Contraction Design for Small Low-Speed Wind Tunnels. August 1988.
[31] B. Cukurel, C. Selcan, T. Arts, Color theory perception of steady wide band liquid crystal thermometry, Exp. Thermal Fluid Sci. 39 (2012) 112–122.
[32] S.J. Kline, F.A. McClintock, Describing uncertainties in single sample experiments, Mech. Eng. 75 (1) (1953) 3–8.
[33] V. de Brederode, P. Bradshaw, Three-Dimensional Flow in nominally Two-Dimensional Separation Bubbles: 1. Flow Behind a Rearward-Facing Step. Imperial College of Science and Technology, Dept. of Aeronautics, London, England, 1972
[34] V.A. Zukauskas, K.A. Pedisius, Heat transfer to reattached fluid flow downstream of a fence, Wärme- und Stoffübertragung 21 (1987) 125–131.
[35] B. Cukurel, C. Selcan, T. Arts, Film cooling extraction effects on the aero-thermal performance of rib roughened cooling channel flow, ASME J. Turbomach. 135 (2) (2013).
[36] B. Cukurel, T. Arts, Local heat transfer dependency on thermal boundary condition in ribbed cooling channel geometries, J. Heat Transfer-Trans. Asme 135 (10) (2013).
[37] K. Inaoka, K. Kakamura, M. Senda, Heat transfer control of a backward-facing step flow in a duct by means of miniature electromagnetic actuators, Int. J. Heat Fluid Flow 25 (2004) 711–720.
[38] K.B. Chun, H.J. Sung, Visualization of a locally-forced separated flow over a backward-facing Step, Exp. Fluids 25 (1998) 417–426.
[39] L.W. Sigurdson, A. Roshko, Controlled unsteady excitation of a reattaching flow, in: AIAA Shear Flow Control Conference, Boulder Colorado, 1985.